Lawrence Berkeley National Laboratory

Title
Solid Electrolyte Bimodal Grain Structures for Improved Cycling Performance

Permalink
https://escholarship.org/uc/item/5fr1b5vk

Journal
Advanced Materials, 36(18)

ISSN
0935-9648

Authors
Jia, Zhanhui
Shen, Hao
Kou, Jiawei
et al.

Publication Date
2024-05-01

DOI
10.1002/adma.202309019

Copyright Information

Peer reviewed

1

Solid Electrolyte Bimodal Grain Structures for

Improved Cycling Performance

3

Zhanhui Jia[1#], Hao Shen[1#*], Jiawei Kou[1], Tianyi Zhang[1], Zhen Wang[1,2], Wei Tang[1,2*],

Marca Doeff[3], Ching-Yu Chiang[4], Kai Chen[1*]

6

1. Center for Advancing Materials Performance from the Nanoscale (CAMP-Nano),
   State Key Laboratory for Mechanical Behavior of Materials, Xi'an Jiaotong
   University, Xi'an, Shaanxi 710049, China
2. School of Chemical Engineering and Technology, Xi'an Jiaotong University, Xi'an,
   Shaanxi 710049, China
3. Energy Storage and Distributed Resources Division, Lawrence Berkeley National
   Laboratory, Berkeley, CA 94720, USA
4. National Synchrotron Radiation Research Center, Hsinchu 30076, Taiwan, ROC

15

These authors contributed equally: Zhanhui Jia, Hao Shen.

E-mail addresses: kchenlbl@gmail.com (K. Chen), shenhao0231@gmail.com (H.

Shen), and tangw2018@xjtu.edu.cn (W. Tang)

19

Abstract

The application of solid-state electrolytes in Li batteries has been hampered by the occurrence of Li-dendrite-caused short circuits. To avoid cell failure, the electrolytes can only be stressed with rather low current densities, severely restricting their performance. Since grain size and pore distributions significantly affect dendrite growth in ceramic electrolytes like $Li_7La_3Zr_2O_{12}$ and its variants, here we have proposed a "detour and buffer" strategy to bring the superiority of both coarse and fine grains into play. To validate the mechanism, a coarse/fine bimodal grain microstructure was obtained by seeding unpulverized large particles in the green body. The rearrangement of coarse grains and fine pores was fine-tuned through changing the ratio of pulverized and unpulverized powders. The optimized bimodal microstructure, obtained when the two powders are equally mixed, allowed, without extra interface decoration, cycling for over 2000 h as the current density was increased from 1.0 $mA \cdot cm^{-2}$ gradually up to 2.0 $mA \cdot cm^{-2}$. The "detour and buffer" effects was confirmed from postmortem analysis. The complex grain boundaries formed by fine grains discourage the direct infiltration of Li. Simultaneously, the coarse grains further increase the tortuosity of the Li path. Our study sheds light on the microstructure optimization for the polycrystalline solid-state electrolytes.

Keywords:

LLZO solid-state electrolyte; bimodal microstructure; Li dendrite suppression; cycling performance; detour and buffer effects

Introduction

The deployment of solid-state electrolytes (SSEs) in all-solid-state Li batteries presents a compelling opportunity due to their nonflammability and compatibility with Li metal, and thus can potentially meet increasing demands for higher energy density and better safety[1, 2]. Among the various SSEs, $Li_7La_3Zr_2O_{12}$ (LLZO), which is doped with Al, Ga, Ta and so on to stabilize the cubic structure, exhibits high ionic conductivities (10^{-4} to 10^{-3} S·cm^{-1}), a wide operating voltage window, and excellent elastic and shear moduli[3]. These make LLZO attractive for use in batteries, but a formidable obstacle still exists: Li dendrites (filaments) form easily and eventually cause short-circuit failure to the cells during electrochemical cycling when a certain critical current density (CCD) is exceeded. The CCD values of SSEs are on the order of hundreds μA at room temperature and much lower than those of liquid electrolytes[4-6], leading all-solid-state Li batteries to operate at low rates. Therefore, circumventing Li dendrites at increased current densities is essential to obtain satisfactory performance on commercially applicable all-solid-state Li batteries.

The exact mechanism of dendrite growth in SSEs remains elusive[7, 8], prompting various strategies to enhance all-solid-state Li battery performance, such as improving Li wettability on the interface[9-12], boosting the Coble creep of Li[13, 14], and adjusting the ratio of ionic and electrical conductivity in SSEs[15, 16]. Besides interface and transport modification, the intrinsic polycrystalline ceramic nature of LLZO SSEs suggests that microstructures such as grain size, grain boundaries, and pores are closely relevant to Li dendrite growth and CCD[17-24]. Consequently, designing and optimizing these microstructures are crucial to improving the cycling properties of SSEs.

Recent studies have shown that fine-grained solid electrolytes, featuring higher grain boundary densities and isolated pores[25], effectively disperse currents and enhance interfacial contacts, allowing higher current densities[26, 27]. However, such almost straight grain boundary microstructures offer insufficient barriers to Li dendrite growth[28, 29] (Figure 1a), limiting the CCD of fine-grained SSEs to below 1 mA·cm^{-2} [20, 30-32]. Additionally, the processing window for SSEs with normally distributed fine grains is narrow[33, 34]. The low energy barrier for sintering fine powders means that grains grow easily. Randomly distributed abnormal grain growth and loose grain boundaries are often observed due to the different mass diffusion rate between grains

74 (In general the larger the grains, the faster they grow). A highly densified structure
75 with Ostwald ripening and grain coarsening can occur when the sintering time is
76 prolonged. Even though coarse grains can provide higher ionic conductivity, the loss
77 of grain boundary complexity, usually accompanied with large interconnected pores
78 encourage Li-dendrite growth[22, 35] (Figure 1b). Consequently, neither fine nor coarse
79 grains solely can effectively promote the electrochemical cycling performance of
80 LLZO SSEs, since both have pros and cons.

81   To solve this dilemma, we adopted a "bimodal" strategy to the fabrication of
82 dense LLZO samples. As shown in Figure 1c, by seeding unpulverized powders (mean
83 diameter of approximately 20 – 30 μm) into the green body with submicron-sized
84 pulverized powders, we achieved inhomogeneous grain growth during the sintering
85 process. The result was a microstructure with bimodally distributed grain sizes. Fine
86 grains filled in the gaps between coarse ones, so that large interconnected pores are
87 effectively avoided. The microstructure with a bimodal grain size distribution, together
88 with finely dispersed pores, increased the tortuosity of Li dendrite paths resulting in a
89 "buffer and detour" effect. As a result, without any additional interface modifications,
90 the LLZO electrolytes with the bimodal microstructure operated stably at current
91 densities higher than 1 mA·cm^{-2} for more than 2000 hours, and successfully cycled
92 more than 100 hours at a current density of 2 mA·cm^{-2}. Our results shed light on the
93 rational design of the SSE microstructures and advancement of cycling performance of
94 the all-solid-state Li batteries.
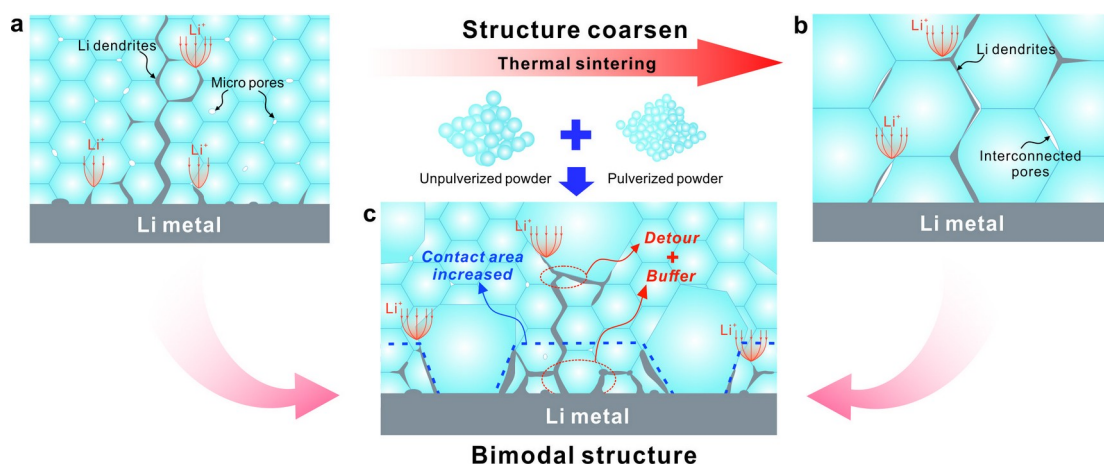
95 **Figure 1. Illustration of polycrystalline SSE with different grain size distributions.**
97 (a) Li dendrites propagate along relatively straight pathways inside the fine-grained SSE.
98 (b) Interconnected pores encourage Li dendrite growth in the SSEs with coarse grains. (c)
99 Expected "detour and buffer" effects to suppress Li dendrite growth in SSE with the

100 bimodal grain microstructure.
101

102 **Experimental**

103 **Synthesis of LLZO powder**

104   The Al-doped LLZO powders were synthesized using a sol-gel method,

105 employing $LiNO_3$ (AR, 99%; Aladdin), $Al(NO_3)_3 \cdot 9H_2O$ (AR, 99.0%; Aladdin),

106 $La(NO_3)_3 \cdot 6H_2O$ (AR, 99.0%; Aladdin), and $ZrO(NO_3)_2 \cdot xH_2O$ (99%; Sigma-Aldrich) as

107 precursors. An extra 14wt% $LiNO_3$ was added to offset any Li loss during the sintering

108 process. These constituents were dissolved in a mixture of deionized water and citric

109 acid. The resultant solution was boiled at 150 °C and then heated to 400 °C to form a

110 uniform brown foam. This foam was crushed in an agate mortar and calcined at 750

111 °C for 2 h in an Al crucible to produce Al-doped LLZO powder with the cubic

112 structure.

113

114 **Fabrication of bimodal LLZO pellets**

115   The synthesized LLZO was sieved into two aliquots of fine and coarse powders.

116 The fine powder was ball-milled at 400 rpm for 30 min and then air-dried. The

117 particle size was measured using an Omic laser particle analyzer for unpulverized

118 coarse powders and a Malvern Zetasizer Nano ZSE particle analyzer for pulverized

119 fine powders. The size distributions of both powders are shown in Figure S1, having

120 median diameters of 0.95 μm and 26.8 μm, respectively. Subsequently, the pulverized

121 and unpulverized powders were mixed in specific weight ratios and pressed into pellets

122 of 13 mm diameter. The weight percent of the unpulverized coarse powder in the

123 green bodies were adjusted to 0%, 25%, 50%, 75%, and 100% for comparative

124 analysis. These green bodies were sintered at 1180 °C for 6 h in Ar atmosphere to

125 achieve densification. The densified pellets, denoted CP0, CP25, CP50, CP75, and

126 CP100, respectively, were polished with sandpaper to clean the surface and eliminate

127 potential surface impurities. The final LLZO pellets had a thickness of 850 μm and a

128 diameter of approximately 10 mm.

129

130 **Microstructure characterizations**

131   The phase purity of the LLZO was ascertained using a Shimadzu XRD-6100

132   diffractometer equipped with Cu Kα radiation. The synthesized LLZO powders and

133   densified pellets were examined using scanning electron microscope (SEM) equipped

134   with X-ray energy dispersive spectroscopy (EDS). A lab-based X-ray computed

135   tomography (CT, Zeiss Xradia 610 Versa) was employed to analyze the pores in the

136   densified LLZO pellets. The X-ray energy was set to 140 keV to ensure sample

137   penetration. The voxel dimension, based on the setup, was 1.4-1.5 μm. More than 990

138   slices were collected for each sample, and tomographic reconstruction was performed

139   using Avizo software from FEI.

140   Synchrotron X-ray nano-Laue-diffraction (nano-Laue) experiments were

141   conducted on Beamline 21A at Taiwan Photon Source (TPS). A polychromatic X-ray

142   beam (5 - 30 keV) was focused to 100×100 nm^2. The LLZO samples were mounted

143   on a scan stage 45° oblique to the incident X-ray. The built-in SEM was utilized to

144   locate the areas of interest. An area of 900×900 μm^2 was scanned with a step size of

145   5 μm on each sample. At each scanning position, a Laue diffraction pattern was

146   recorded in reflection mode with a 2D detector situated 90° to the X-ray beam, and the

147   fluorescence signals of Zr, Al and La were collected using a Si-drift detector

148   concurrently. The Laue patterns were analyzed using a custom-developed algorithm[36,

149   37] to map the crystal grain distribution on the sintered LLZO.

150

151   **Electrochemical tests**

152   Ionic conductivity was measured via electrochemical impedance spectroscopy

153   (EIS) tests. 10 mV AC voltage (0.1 Hz to 1 MHz) was applied at room temperature

154   using a PARSTAT MC multichannel workstation. The top and bottom surfaces of the

155   LLZO pellets were sputter coated with Pt as blocking electrodes.

156   Li symmetric cells were fabricated by affixing a Li foil on both sides of the

157   LLZO pellets and assembling 2032-type coin cells in a glovebox. The Li foils were 8

158   mm in diameter and 600 μm thick. To secure the contact with Li metal, the assembled

159   coin cells were annealed at 150 °C for 10 min. Galvanostatic and CCD tests were

160   conducted using a Neware BTS 4000 at room temperature.

161

162   **Results**

163   X-ray diffraction analyses of the synthesized LLZO powder are consistent with a

164 cubic phase in the space group Ia-3d (Figure S2a). Minor impurities, primarily $LiAlO_2$

165 and $LaAlO_3$, were detected in the LLZO powder, mainly due to the locally

166 inhomogeneous chemical reaction. These impurities, as shown in Figure S3, will be

167 eliminated during the sintering process, and thus their effects are ignored in this study.

168 The morphology and chemical distributions of both types of powders are displayed in

169 Figure S2b to S2f.

170   After sintering, all the samples, CP0 to CP100, are well-densified and retain the

171 cubic structure (Figure S3). Their relative densities are listed in Table S1. The

172 microstructural characteristics of the post-sintered samples, from CP0 to CP100, were

173 investigated using nano-Laue. Combining the diffraction peak intensity and grain

174 maps plotted in Figure 2a and b, which depict the microscopic defect density and

175 crystal orientation distributions[38, 39], CP0 exhibits a normally distributed grain size

176 across the scanned area and does not have a bimodal microstructure, with limited

177 number of pores among the grains. CP25, CP50, and CP75 display increasing area of

178 fine grains (indicated by the mosaic regions) adjacent to the large ones. Considering

179 that each pixel in the map represents an area of 5×5 μm^2, most of the fine grains

180 within the mosaic regions are less than 10 μm. CP100 exhibits the largest grains and

181 pores.

182   Subsequently, the sizes of coarse grains were measured quantitatively after

183 filtering fine grains and pores. Pixels within an individual coarse grain were counted to

184 calculate the area and equivalent diameter. As illustrated in Figure 2c, the area fraction

185 of coarse grains initially decreased when the ratio of unpulverized powders in the

186 green body rose to 50%. However, it increased in CP75 and dropped again in CP100.

187 In the statistical analysis (Figure 2d, with total number of measured coarse grains

188 exceeding 100 for each sample), the grain size of all tested samples was predominantly

189 below 120 μm. Specifically, in CP50, grain growth appears inhibited, resulting in the

190 lowest median grain size among the five samples. The number of grains sized larger

191 than 120 μm and smaller than 200 μm reduced as the ratio of unpulverized powder

192 increased from 0 to 50%; however, in CP75 and CP100, there was more abnormal

193 grain growth with sizes exceeding 200 μm.

194   The SEM images of the fracture surfaces of CP25, CP50, and CP75 (Figure 2e)

195 indicate that the coarse grains are surrounded by fine ones, with CP50 displaying the

196 densest structure. As shown in Figure 2f, slight element segregation was observed
197 between grains. The grey color in the maps are the pores. Areas enriched with La have
198 less Zr, an effect attributed to Li excess[40].
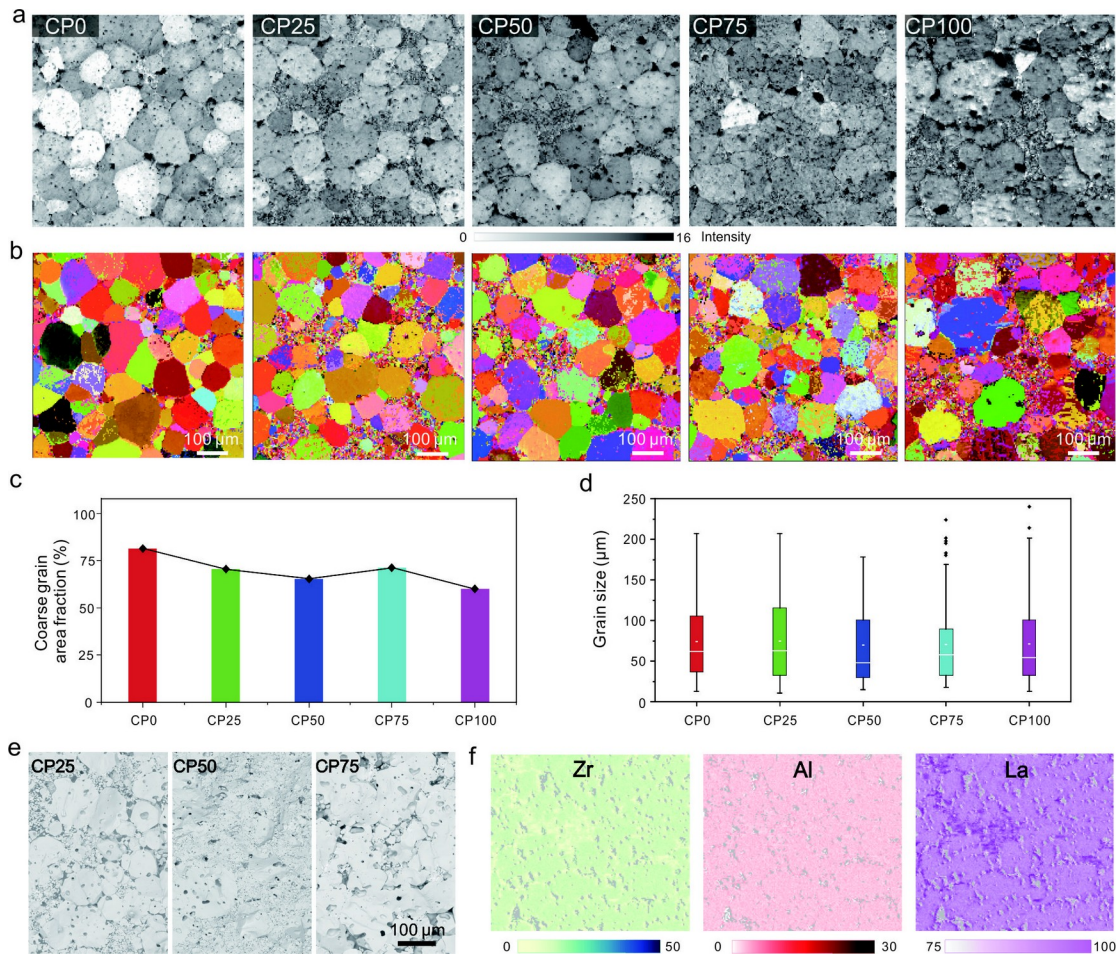
199

200 **Figure 2. Grain study of LLZO with bimodal arrangement.** Nano-Laue analyzed grain
201 distribution as shown in (a) intensity map and (b) color-labeled orientation map. (c) Area
202 fraction of coarse grains in all five samples. (d) Box chart of coarse grain size
203 distribution, red line and black dots inside the boxes indicate the mean and median,
204 respectively. (e) SEM-BSE images of the cross-sectional morphology. (f) X-ray
205 fluorescence maps on the same nano-Laue scanned area of CP50.
206

207 The influence of the bimodal microstructure on pore morphology and
208 distribution within the densified LLZO was investigated using CT. A $431 \times 453 \times 293$
209 μm^3 volume was selected from a similar position in each fabricated sample for
210 comparison. In Figure 3a, by labelling adjacent pores with distinct colors, it is clear
211 that CP0 features large and interconnected pores, while the pores are mostly isolated
212 in the samples from CP25 to CP100. In Figure 3b, where the translucent-scarlet shades
213 are employed to represent pore volume distribution, the scarlet color is hardly

observed in CP50, proving that pore growth and coalescence was suppressed. Furthermore, CP50 possesses the smallest total pore volume (1.78×10^6 µm^3) among all five samples, whereas the total number of pores in CP25, CP50 and CP75 are similar (Figure 3c). Although CP0 has the least number of pores, CP50 is the densest structure (95.1% density, Table S1). In the violin plot (Figure 3d), pore size distribution is better visualized. CP50 demonstrates the narrowest pore size distribution, averaging at 7.2 µm. Even though CP100 has the lowest average pore size (4.3 µm), a number of large pores (> 40 µm) still exist, resulting in the lowest density among all five samples.
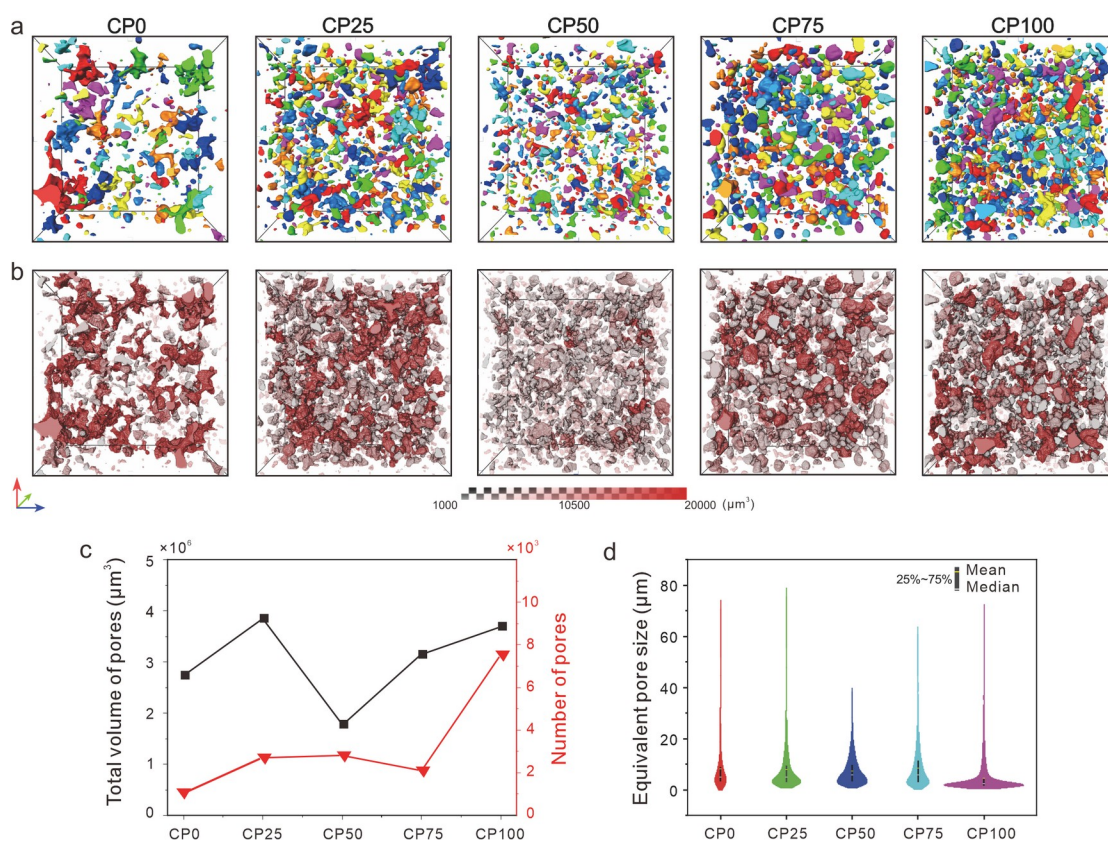
Figure 3. Pore rearrangement and morphology study of LLZO samples with bimodal structures. (a) Morphology and distribution density of the pores are observed using lab-based CT in sequence, with sampling volume of $431 \times 453 \times 293$ µm^3. (b) Translucent-scarlet shades are employed to show pore volume distribution and connectivity in each sample. The evolution of (c) total volume, population and (d) equivalent size are statistically studied in each sample.

For room-temperature electrochemical tests, all LLZO pellets underwent similar polishing processes to minimize artificial effects. The pellets were then sandwiched between Li electrodes under consistent pressure and heated at 150 °C for 10 min to

234   fabricate symmetric cells. As revealed in the Nyquist plot (Figure 4a), the curves

235   consist of one partial semicircle in the high-frequency range and flattened semicircles

236   at lower frequencies. The high-frequency semicircles represent the total resistance of

237   the LLZO pellets, while the lower-frequency impedances are attributed to the

238   resistances at the Li/LLZO interfaces[41,42], which is mainly due to the interface

239   morphology caused constriction resistance and charge transfer resistance[43,44]. The

240   measured total conductivities of all samples are about the same order of magnitude,

241   ranging from 2 to 4×10^{-4} S·cm^{-1} (see Table S1). The impedance data are fitted and

242   presented as continuous curves, and the fitted resistances are listed in Table S2.

243   Generally, from CP0 to CP50, the interface resistance drops from 603 to 203 Ω·cm^2.

244   In CP50, the combined effects of more fine grains, fewer pores, and smaller pore size

245   contribute to the decrease of both constriction resistance and charge transfer

246   resistance. The decreased coarse grain fraction promotes charge transfer properties,

247   which has been corroborated by previous reports[26]. In contrast, in CP75, the presence

248   of abnormally-grown grains and increased volume fraction of pores leads to increased

249   constriction and charge transfer resistance. As a result, the interface impedance of

250   CP75 is several times higher than that of the CP50. CP100 exhibits a relatively low

251   constriction resistance but high charge transfer resistance, probably because most

252   pores in it are small (Figure 3d), while the abnormal growth of grains is not

253   prohibited. Additionally, the bulk resistances of CP25, CP75 and CP100 are high,

254   because of their increased pore volume fractions that increase the tortuosity of Li

255   transfer path[45]. Apart from decreasing interfacial resistance, the optimal bimodal

256   microstructure plays a significant role in enhancing the cycling behavior. Figure 4b

257   shows DC stepped current cycling of the symmetrical cells containing CP50. The

258   current density was raised to as much as 1.1 mA·cm^{-2} at 25 °C, without causing any

259   detectable hard short. When the CP50 sample was thinned to 500 µm, the critical

260   current density was further elevated to 1.6 mA·cm^{-2} (see Figure S4, SEM, impedance

261   and cycling test results of this sample are also presented). The voltage drops are not

262   proportional to current densities (Figure S5), indicating the drop of cell resistance,

263   probably because Li infiltrates into LLZO and fulfills the pores on/near the interfaces

264   during the stripping and plating processes[46-48]. This is equivalent to the reduction of the

265   LLZO thickness and the improvement of interface contact. Another possible

266 explanation to the lowered resistance might be the modification of solid electrolyte

267 interphase via passage of current, making it less resistive[49].

268   To assess the stability of the interfaces, cells were subjected to galvanostatic

269 charging and discharging at a consistent temperature of 25 °C. Each half-cycle lasted

270 30 min. For a holistic comparison, all symmetric cells from CP0 to CP100 were tested

271 and exhibited significant differences in cycling stability under a low current density of

272 ± 0.1 mA·cm^{-2} (Figure S6). As depicted in Figure 4d, the galvanostatic profile of the

273 Li/CP50/Li symmetric cell displayed an initial potential of approximately ± 90 mV,

274 which subsequently dropped to around ± 50 mV, cycling steadily over 1000h,

275 outperforming all others. The decrease in potential indicates that Li penetrates into

276 LLZO, forming a stable interface post activation cycles[46]. When further cycling the Li/

277 CP50/Li symmetric cell at a current density of ± 0.3 mA·cm^{-2}, the cell voltage

278 remained at ~70 mV for an extended cycling period of up to 1000 h. Another sample

279 experienced a quick increase in current density. Remarkably, stable cycling was

280 successfully achieved on it at high current densities of 1 mA·cm^{-2} and 1.2 mA·cm^{-2}

281 (Figure 4e) for approximately 2000 h. In a previously reported system that showed a

282 similar voltage profile to those in Figure 4f and 4g, Li filaments were observed inside

283 LLZO, but their growth was reversible and cyclable[50]. Subsequently, as the current

284 density was increased stepwise in units of ± 0.1 mA·cm^{-2} from ± 1.2 mA·cm^{-2} to ± 2.0

285 mA·cm^{-2} with each increment lasting 100 h (Figure 4h1-h8), the voltage profile

286 remained similar to that observed at lower current densities. As the current density

287 increased, the deviation of the voltage profile from the expected square shape became

288 more severe, suggesting that Li was stripped faster at the interface than it could diffuse

289 from the bulk to compensate the stripped Li. The cycling started to lose stability with

290 an obvious voltage drop (Figure 4e, see voltage profile between h7 and h8) when the

291 current density was approximately 1.8 mA·cm^{-2}, due to soft shorting; however, the

292 symmetric cell did not fail even at 2.0 mA·cm^{-2}. This suggests that the bimodal

293 structure of CP50 prevented the propagation of Li filaments/dendrites or healed them,

294   ensuring robust cycling. With another CP50 symmetrical cell, the evolution of the

295   impedances as a function of cycles was investigated. As displayed in Figure S7, the

296   cell (Cell #1) was cycled with the current densities ramping up in a stepwise manner

297   from 0.3 to 1 $mA \cdot cm^{-2}$ (Figure S7a). At 0.3 $mA \cdot cm^{-2}$, the interface resistance first

298   decreased and then stabilized in the following cycles, as shown in Figure S7b and c.

299   As the current density was increased from 0.3 to 0.8 $mA \cdot cm^{-2}$, the impedance became

300   lower (Figure S7d), indicating that more Li had infiltrated into LLZO. The evolution

301   of solid electrolyte interphase might also play a role. Soft shorting was detected from

302   the impedance curve measured after 16 cycles at 1 $mA \cdot cm^{-2}$. Afterwards, the

303   impedance became unstable and dropped down rapidly (Figure S7e). In another

304   symmetrical cell (Cell #2), the cycling current density was increased from 0 to 1.0

305     $mA \cdot cm^{-2}$ in 10 cycles, kept constant at 1.0 $mA \cdot cm^{-2}$ for 50 cycles, ramped up in a

306   stepwise manner to 1.8 $mA \cdot cm^{-2}$ and finally kept at 1.8 $mA \cdot cm^{-2}$ for 77 cycles (Figure

307   S8a). The evolution of impedance during the 50 cycles at 1.0 $mA \cdot cm^{-2}$ and 77 cycles at

308   1.8 $mA \cdot cm^{-2}$ was quite similar to that in Cell #1 under 0.3 $mA \cdot cm^{-2}$. The impedance

309   dropped slightly at the beginning and then reached a stable state after about 40 cycles

310   (Figure S8b).

311
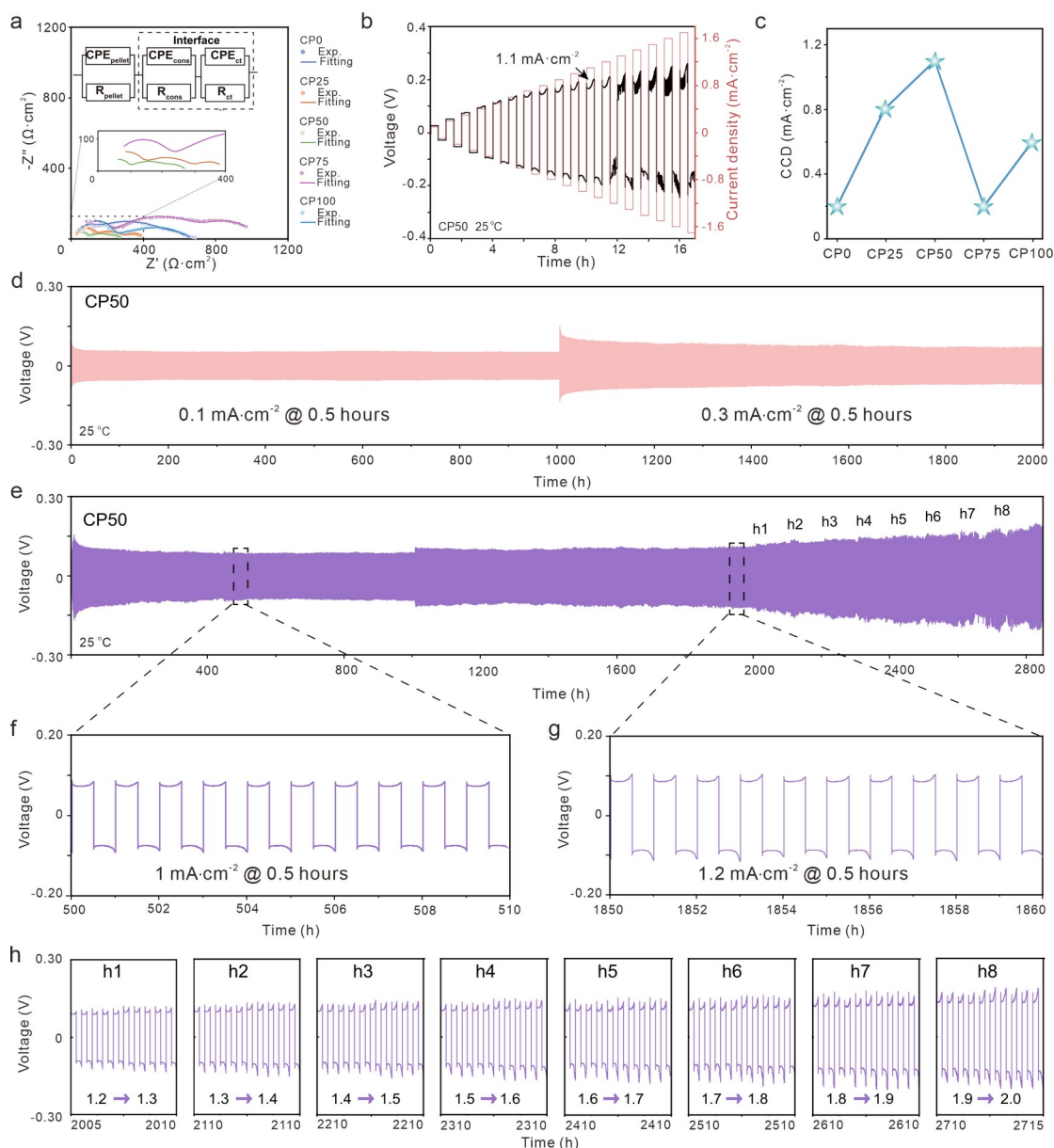
Figure 4. Electrochemical performance of the symmetric cells containing bimodal microstructured LLZO. (a) The ionic conductivity of Li symmetric cells containing samples with various types of bimodal microstructures was studied using EIS. (b) The CCD of the symmetric cell containing CP50 was measured by increasing the current stepwise and (c) a comparison of the CCD of cells containing the different samples. (d, e) Voltage profiles of the CP50 symmetric cells cycled under increased current densities, with zoom-in details shown in (f-h).

The cells containing CP50 outperform in every aspect, be it CCD (Figure 4c), overpotential, or cycling lifetime. For reference, the cycling stability and CCD test results for symmetric cells containing other bimodal microstructures are displayed in Figure S6 and Figure S9. Importantly, the interfaces in the tested cells are unadorned, i.e., free of any additional coatings. As demonstrated in Figure 5, the outcomes from

326 our CP50 specimens not only outperform the previously reported symmetric cells

327 without interface and/or grain boundary decoration (in the blueish-grey area), but also

328 surpass or at least run on a par with those incorporating interface modifications (in the

329 yellow region).
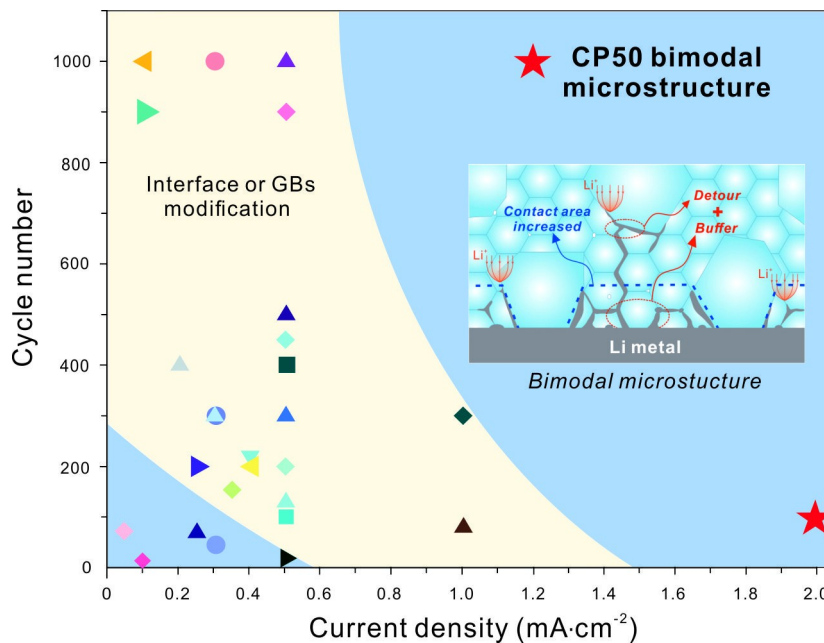
330

331 **Figure 5. Galvanostatic cycling performance of Li symmetric cells with bulky**
332 **garnet-type solid electrolytes (references are listed in Table S3).**

333

334 **Discussion**

335 **The formation of bimodal microstructure**

336 The bimodal microstructure was obtained by sintering a mixture of pulverized

337 and unpulverized powders. In the mixed state, small particles fill the interstices

338 between the large ones. During sintering, the inhomogeneous powder distribution

339 results in non-uniform mass diffusion. The intra-agglomerate densification and grain

340 growth occur in unpulverized powders more easily and rapidly, which consume the

341 mass that is necessary for the pulverized fine powders to grow[51]. Moreover, sintering

342 also influences the size, morphology, and spatial distributions of pores. As small

343 particles coalesce, small pores are easily formed between them. On the other hand,

344 when there are more large particles, more intragranular pores are trapped and cannot

345 escape from the interior to the surface of the powder. According to experimental

346 observations, grain growth takes place under the regular coarsening process in CP0,

347 forming normally distributed coarse grains with large interconnected pores. CP25 has

348 more isolated pores but still suffers adverse effects from the interconnected ones. In

349 CP75 and CP100, the unpulverized coarse powders become the principal component

350 in green bodies, and the fast grain growth and fine grain consumption lead to more

351 abnormal large grains. In CP50, a synergy is achieved, as the competing grain growths

352 of unpulverized and pulverized powders are balanced. The coarse grains grow in a

353 constricted manner, sparing the fine grains opportunities to sinter well. Additionally,

354 the presence of excess Li can cause more pores to form[40, 52], because gas is entrapped

355 between particles during the rapid densification and volatilization of the Li-containing

356 compounds employed to replenish Li loss. It should be noticed that the adding of Li-

357 containing compounds which melt at low temperature, such as $LiNO_3$ and Li_2CO_3, can

358 boost densification due to liquid-phase sintering. In summary, the initial powder size,

359 grain growth rate, as well as Li excess affects the size and spatial distributions of

360 pores.

361 With these observations, we surmise that a balanced ratio of pulverized and

362 unpulverized powders, as in CP50, facilitates a bimodal microstructure of uniformly

363 distributed coarse grains encapsulated by fine grains. Small and isolated pores, as well

364 as a dense structure, are also obtained. Three guiding principles can be summarized

365 for microstructure control concerning particle size effects in the green body: (1)

366 adjacent large grains and rapid grain growth in polycrystalline SSE tend to create

367 interconnected pores and intragranular pores; (2) introducing a certain size of large

368 particles into the green body can significantly reduce interconnected pores via

369 differential densification; (3) by controlling the ratio of two different types of powders,

370 the size and population of pores can be adjusted, regardless of whether they are

371 between or inside grains.

372

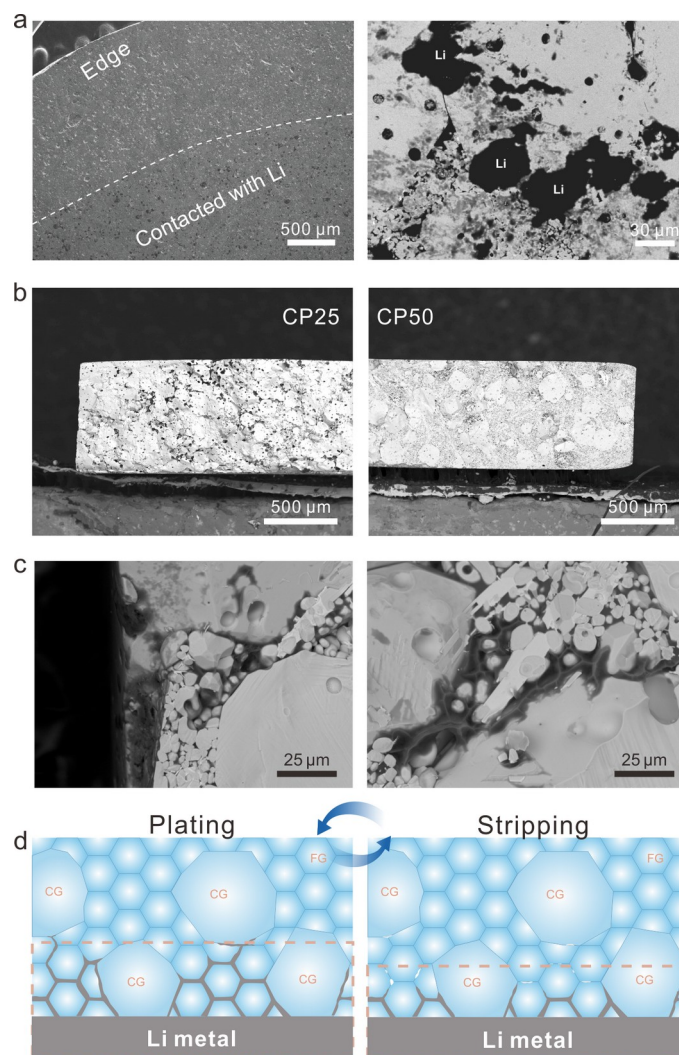373 **Buffer and detour effects in bimodal microstructure**

374 After cycling, the cells were disassembled to examine Li deposition behavior

375 within the bimodal microstructure. Figure 6a shows the interface that distinguishes

376 between areas with and without Li foil contact. As the Li foil diameter is 2 mm

377 smaller than LLZO, the periphery not in contact with Li is clean, while the dark spots

378 signify the existence of Li under back-scattered electron mode of the SEM image[35, 53].

379 Magnified images reveal prominent Li deposition within grain boundaries and pores.

380 In Figure 6b, widespread dark color is readily detected in CP25, indicating
381 conspicuous Li propagation due to the detour effect primarily caused by coarse grains.
382 In contrast, dark spots are barely seen in CP50 due to the considerable area fraction of
383 fine grains, leading to a finer and more complex Li propagation path. However, upon
384 closer examination (Figure 6c), it can be seen that Li propagation in the fine grain area
385 forms a net-like distribution. The fine grain areas, as well as fine pores, even those that
386 are submicron size, act as Li metal reservoirs, thereby enhancing cycling stability
387 under high current densities due to its buffering effect.

388   In recent studies, the presence of pores has been identified as one of the key
389 factors for Li dendrite initiation and propagation[17, 54, 55]. The size and distance between
390 the pores and interfaces affect the current density that the SSE is able to withstand.
391 Reducing the size and quantity of pores at the subsurface, and preventing the build-up
392 stress caused by Li-filled pores from exceeding the local fracture toughness has been
393 shown to be beneficial. Our bimodal microstructure design is consistent with this
394 strategy. The introduction of coarse grains reduces subsurface pores and the chances
395 of Li dendrite contact. Coarse LLZO grains with lower defect densities provide higher
396 fracture toughness and thus can withstand higher current density. Furthermore, the
397 size of subsurface pores is effectively reduced by the bimodal microstructure in which
398 fine grains surround coarse ones, bringing the Li-pore-filling induced pressure to a
399 magnitude far below the fracture toughness. Additionally, the pores along LLZO grain
400 boundaries have the chance to form interconnected channels, which further lowers the
401 pressure during plating. The benefit of the microstructure is that crack initiation is
402 circumvented; even if cracking occurs, it consumes the energy for crack propagation
403 and prevents hard shorts.

404   Generally, the reasons for the enhanced cycling stability in bimodal SSE can be
405 divided into two aspects: (1) the fine grains surround the coarse ones, eliminating the
406 interconnected pores and providing a zigzagging propagation pathway to hamper the
407 direct and rapid infiltration of Li. In the meantime, the coarse grains lying on the
408 infiltration route of Li detours its migration and delays the failure of SSEs; (2) pores
409 filled with Li aid in moving the Li/LLZO interface forward, significantly increasing
410 the Li contact area, thereby dispersing the interfacial current and facilitating uniform
411 and reversible stripping and plating cycles (Figure 6d). This mitigates the void

formation and contact loss at the interface caused by high current density. Such improvements contribute to all-solid-state Li battery cycles without necessitating additional mechanical pressure for accelerating Li creep, which is deleterious to long-term cycling[17].

Figure 6. Postmortem analysis of Li deposition after electrochemical cycling. SEM-BSE images of (a) LLZO surface morphology and (b) cross-section after short circuit. (c) Li network propagation between the fine grains. (d) Schematic illustration of Li network infiltration between fine grains and in pores pushing the interface forward.

On the LLZO surface, we also notice spallation cracks (Figure S10), predominantly around the pores in the coarse grain areas and along the grain boundaries where large wedges are not entirely filled with fine grains. These cracks are caused by stress buildup during the pre-filling procedure of viscoelastic Li metal[54, 55]. This suggests two aspects of future microstructure control. The intra-granular pores

427   should be minimized in both quantity and size, which can be achieved by reducing the

428   excess Li in the green body and curtailing the growth rate of coarse grains. Fine grains

429   should also be more tightly packed around the coarse grains.

430

431   **Conclusion**

432   In conclusion, our study focuses on the microstructure design and optimization of

433   polycrystalline LLZO SSEs to enhance cycling performance, incorporating both CCD

434   and long-term cycling stability. By mixing pulverized and unpulverized powders into

435   the green body, a bimodal microstructure was obtained. Tuning the ratio of these two

436   types of powders allows for the alteration of the distribution of grains and pores in the

437   sintered samples, and thus influences the electrochemical properties significantly.

438   When the pulverized and unpulverized powders are equally mixed, a microstructure in

439   which coarse grains are surrounded by fine-grains and isolated fine pores are obtained,

440   which results in efficient Li plating/stripping at a high current density. Long-term

441   cycling stability experiments underscore the exceptional stability of symmetric cells

442   containing the LLZO SSEs with the optimal bimodal microstructure, over 2000 h at

443   current densities of 1.0 $mA·cm^{-2}$ and 1.2 $mA·cm^{-2}$. It even exhibits the capacity to

444   endure over 100 h under a current density of 2 $mA·cm^{-2}$.

445   Postmortem analysis reveals that intricate grain boundaries, formed by the fine

446   grains in the bimodal structure, make the Li penetration path more complex, thereby

447   reducing direct Li infiltration. Simultaneously, the coarse grains enhance the tortuosity

448   of the Li path. With the "buffer and detour" effects, the LLZO electrolyte gains the

449   potential to operate at elevated current densities. The propensity of Li to permeate

450   between fine grains indirectly propels the interface forward, promoting reversible Li

451   stripping and plating, and showcasing excellent cycling stability. Spallation cracks,

452   primarily surrounding the pores in coarse grains and the edges of coarse grains

453   without full contact with fine grains, are detected at the interface. These observations

454   hint at future opportunities for microstructure optimization. In the realm of battery

applications, it is also essential to investigate the compatibility of the solid-state electrolytes with the cathode electrodes. This involves a thorough consideration of cathode materials, additives, interfacial decorations, and cathodic composite structure design. Our findings illuminate the path to rational and optimal design of bimodal structures, offering new insights on mitigating dendrite growth-induced failure in polycrystalline SSEs.

References

1. J. Janek, W. G. Zeier, *Nat. Energy.* **2016**, 1, 1.
2. Q. Zhao, S. Stalin, C.-Z. Zhao, L. A. Archer, *Nat. Rev. Mat.* **2020**, 5, 229.
3. A. J. Samson, K. Hofstetter, S. Bag, V. Thangadurai, *Energy Environ. Sci.* **2019**, 12, 2957.
4. T. Famprikis, P. Canepa, J. A. Dawson, M. S. Islam, C. Masquelier, *Nat. Mater.* **2019**, 18, 1278.
5. J. Janek, W. G. Zeier, *Nat. Energy.* **2023**, 8, 230.
6. M. J. Wang, R. Choudhury, J. Sakamoto, *Joule* **2019**, 3, 2165.
7. T. Krauskopf, F. H. Richter, W. G. Zeier, J. r. Janek, *Chem. Rev.* **2020**, 120, 7745.
8. H. Shen, K. Chen, J. Kou, Z. Jia, N. Tamura, W. Hua, W. Tang, H. Ehrenberg, M. Doeff, *Mater. Today.* **2022**, 57, 180.
9. X. Han, Y. Gong, K. Fu, X. He, G. T. Hitz, J. Dai, A. Pearse, B. Liu, H. Wang, G. Rubloff, *Nat. Mater.* **2017**, 16, 572.
10. R. Dubey, J. Sastre, C. Cancellieri, F. Okur, A. Forster, L. Pompizii, A. Priebe, Y. E. Romanyuk, L. P. Jeurgens, M. V. Kovalenko, *Adv. Energy Mater.* **2021**, 11,

489   2102086.

490   11. N. J. Taylor, S. Stangeland-Molo, C. G. Haslam, A. Sharafi, T. Thompson, M.
491   Wang, R. Garcia-Mendez, J. Sakamoto, *J. Power Sources.* **2018**, 396, 314.

492   12. K. Fu, Y. Gong, Z. Fu, H. Xie, Y. Yao, B. Liu, M. Carter, E. Wachsman, L. Hu,
493   *Angew. Chem., Int. Ed.* **2017**, 56, 14942.

494   13. Y. Chen, Z. Wang, X. Li, X. Yao, C. Wang, Y. Li, W. Xue, D. Yu, S. Y. Kim, F.
495   Yang, *Nature.* **2020**, 578, 251.

496   14. J. Kasemchainan, S. Zekoll, D. Spencer Jolly, Z. Ning, G. O. Hartley, J. Marrow,
497   P. G. Bruce, *Nat. Mater.* **2019**, 18, 1105.

498   15. W. Ping, C. Wang, Z. Lin, E. Hitz, C. Yang, H. Wang, L. Hu, *Adv. Energy Mater.*
499   **2020**, 10, 2000702.

500   16. X. Wang, J. Chen, Z. Mao, D. Wang, *Chem. Eng. J.* **2022**, 427, 130899.

501   17. Z. Ning, G. Li, D. L. Melvin, Y. Chen, J. Bu, D. Spencer-Jolly, J. Liu, B. Hu, X.
502   Gao, J. Perera, *Nature.* **2023**, 618, 287.

503   18. E. J. Cheng, A. Sharafi, J. Sakamoto, *Electrochim. Acta.* **2017**, 223, 85.

504   19. G. Li, C. W. Monroe, *Phys. Chem. Chem. Phys.* **2019**, 21, 20354.

505   20. A. Sharafi, C. G. Haslam, R. D. Kerns, J. Wolfenstine, J. Sakamoto, *J. Mater.*
506   *Chem. A.* **2017**, 5, 21491.

507   21. M. B. Dixit, M. Regala, F. Shen, X. Xiao, K. B. Hatzell, *ACS Appl. Mater.*
508   *Interfaces.* **2018**, 11, 2022.

509   22. F. Shen, M. B. Dixit, X. Xiao, K. B. Hatzell, *ACS Energy Lett.* **2018**, 3, 1056.

510   23. K. Tantratian, H. Yan, K. Ellwood, E. T. Harrison, L. Chen, *Adv. Energy Mater.*
511   **2021**, 11, 2003417.

512   24. H.-K. Tian, Z. Liu, Y. Ji, L.-Q. Chen, Y. Qi, *Chem. Mater.* **2019**, 31, 7351.

513   25. F. Okur, H. Zhang, D. T. Karabay, K. Muench, A. Parrilli, A. Neels, W.
514   Dachraoui, M. D. Rossell, C. Cancellieri, L. P. Jeurgens, *Adv. Energy Mater.*
515   **2023**, 13, 2203509.

516   26. L. Cheng, W. Chen, M. Kunz, K. Persson, N. Tamura, G. Chen, M. Doeff, *ACS*
517   *Appl. Mater. Interfaces.* **2015**, 7, 2073.

518   27. D. K. Singh, A. Henss, B. Mogwitz, A. Gautam, J. Horn, T. Krauskopf, S.
519   Burkhardt, J. Sann, F. H. Richter, J. Janek, *Cell Rep. Phys. Sci.* **2022**, 3, 101043.

520   28. H. Huo, Y. Chen, R. Li, N. Zhao, J. Luo, J. G. P. da Silva, R. Mücke, P.
521   Kaghazchi , X. Guo, X. Sun, *Energy Environ. Sci.* **2020**, 13, 127.

522   29. Q. Dai, J. Yao, C. Du, H. Ye, Z. Gao, J. Zhao, J. Chen, Y. Su, H. Li, X. Fu, J.
523   Yan, D. Zhu, X. Zhang, M. Li, Z. Luo, H. Qiu, Q. Huang, L. Zhang, Y. Tang, J.
524   Huang, *Adv. Funct. Mater.* **2022**, 32, 2208682.

525   30. F. M. Pesci, R. H. Brugge, A. O. Hekselman, A. Cavallaro, R. J. Chater, A.
526   Aguadero, *J. Mater. Chem. A* **2018**, 6, 19817.

527   31. Z. Huang, L. Chen, B. Huang, B. Xu, G. Shao, H. Wang, Y. Li, C.-A. Wang, *ACS*
528   *Appl. Mater. Interfaces.* **2020**, 12, 56118.

529   32. S. Lee, K.-s. Lee, S. Kim, K. Yoon, S. Han, M. H. Lee, Y. Ko, J. H. Noh, W.
530   Kim, K. Kang, *Sci. Adv.* **2022**, 8, eabq0153.

33. J. Su, X. Huang, Z. Song, T. Xiu, M. E. Badding, J. Jin, Z. Wen, *Ceram. Int.* **2019**, 45, 14991.

34. Y. Tian, Y. Zhou, Y. Liu, C. Zhao, W. Wang, Y. Zhou, *Solid State Ionics.* **2020**, 354, 115407.

35. Y. Ren, Y. Shen, Y. Lin, C.-W. Nan, *ACS Appl. Mater. Interfaces.* **2019**, 11, 5928.

36. J. Kou, K. Chen, N. Tamura, *Scr. Mater.* **2018**, 143, 49.

37. G. Zhou, W. Zhu, H. Shen, Y. Li, A. Zhang, N. Tamura, K. Chen, *Sci. Rep.* **2016**, 6, 28144.

38. R. Barabash, G. Ice, B. Larson, G. Pharr, K.-S. Chung, W. Yang, *Appl. Phys. Lett.* **2001**, 79, 749.

39. G. Zhou, J. Kou, Y. Li, W. Zhu, K. Chen, N. Tamura, *Quantum Beam Sci.* **2018**, 2, 13.

40. C. Schwab, G. Häuschen, M. Mann, C. Roitzheim, O. Guillon, D. Fattakhova-Rohlfing, M. Finsterbusch, *J. Mater. Chem. A* **2023**, 11, 5670.

41. H. Buschmann, J. Dölle, S. Berendts, A. Kuhn, P. Bottke, M. Wilkening, P. Heitjans, A. Senyshyn, H. Ehrenberg, A. Lotnyk, *Phys. Chem. Chem. Phys.* **2011**, 13, 19378.

42. L. Zhang, L. Cheng, J. Cabana, G. Chen, M. M. Doeff, T. J. Richardson, *Solid State Ionics* **2013**, 231, 109.

43. S. J. Cooper, A. Bertei, D. P. Finegan, N. P. Brandon, *Electrochim. Acta.* **2017**, 251, 681.

44. J. K. Eckhardt, P. J. Klar, J. Janek, C. Heiliger, *ACS Appl. Mater. Interfaces.* 2022, 14, 35545.

45. M. B. Dixit, M. Regala, F. Shen, X. Xiao, K. B. Hatzell, *ACS Appl. Mater. Interfaces.* 2018, 11, 2022.

46. X. Ji, S. Hou, P. Wang, X. He, N. Piao, J. Chen, X. Fan, C. Wang, *Adv. Mater.* **2020**, 32, 2002741.

47. H. Huo, J. Liang, N. Zhao, X. Li, X. Lin, Y. Zhao, K. Adair, R. Li, X. Guo, X. Sun, *ACS Energy Lett.* **2020**, 5, 2156.

48. B. Kinzer, A. L. Davis, T. Krauskopf, H. Hartmann, W. S. LePage, E. Kazyak, J. Janek, N. P. Dasgupta, J. Sakamoto, *Matter.* **2021**, 4, 1947.

49 Y. Xu, K. Dong, Y. Jie, P. Adelhelm, Y. Chen, L. Xu, P. Yu, J. Kim, Z. Kochovski, Z. Yu, *Adv. Energy Mater.* 2022, 12, 2200398.

50. E. Kazyak, R. Garcia-Mendez, W. S. LePage, A. Sharafi, A. L. Davis, A. J. Sanchez, K.-H. Chen, C. Haslam, J. Sakamoto, N. P. Dasgupta, *Matter.* **2020**, 2, 1025.

51. R. M. German, *Metall. Trans. A* **1992**, 23, 1455.

52. M. N. Rahaman, *Sintering of Ceramics*, CRC press, **2007**.

53. F. Aguesse, W. Manalastas, L. Buannic, J. M. Lopez del Amo, G. Singh, A. Llordés , J. Kilner, *ACS Appl. Mater. Interfaces.* **2017**, 9, 3808.

54. F. Han, A. S. Westover, J. Yue, X. Fan, F. Wang, M. Chi, D. N. Leonard, N. J. Dudney, H. Wang, C. Wang, *Nat. Energy.* **2019**, 4, 187.

573   55. Q. Tu, T. Shi, S. Chakravarthy, G. Ceder, *Matter.* **2021**, 4, 3248.